3D large-deformation modeling of Lomba Grande landslide runout using coupled Eulerian-Lagrangian method

Xuejian Chen[1], Fabricio Fernández[2], Euripides Vargas[3], Carlos Sousa Oliveira[4], Miguel Inácio[4,5], Joao Carlos Nunes[6], Luis Ribeiro e Sousa[7], Ana Malheiro[8], Rita Leal Sousa[1,*]

1 New York University, Abu Dhabi, UAE

2 Universidad Católica del Norte, Antofagasta, Chile

3 PUC-Rio: Pontifical Catholic University of Rio de Janeiro, Brazil.

4 Instituto Superior Técnico/Ceris/University of Lisbon, Portugal.

5 Instituto Dom Luiz, Lisbon, Portugal.

6 Universidade dos Acores, Portugal.

7 University of Porto, Portugal.

8 Regional Civil Engineering Laboratory, Portugal.

* *Corresponding author (E-mail:* rita.sousa@nyu.edu*)*

Abstract: Lomba Grande in the Azores Islands is highly susceptible to geohazards like earthquakes and volcanic eruptions, making slopes prone to landslides. This study models an earthquake-induced landslide at Lomba Grande in three dimensions (3D), using the Coupled Eulerian-Lagrangian (CEL) large-deformation technique, aiming at providing practical geotechnical insights regarding the run-out process of the failed mass after the collapse event. A new empirical geomechanical system explicitly developed for volcanic rocks, the Volcanic Rock System (VRS), is used to classify the rock mass. The VRS indicates that the classification of the rock mass varies between Class VI (Very Poor) and Class V (Poor). A linear baseline correction is conducted on the 1998 Faial Earthquake (Mw 6.2) recorded at the station of Horta, to eliminate residual velocity and displacement. The numerical result reveals that the Lomba Grande landslide was a high kinetic-energy geo-disaster event with fast movement (maximum sliding velocity of 46.1 m/s) and significant plastic dissipation at the interface between the failed mass and the base rock along with the long-distance runout process. Additionally, the runout path of the Lomba Grande landslide is heavily affected by the complex topography, implying that the assumption of an ideal slope without incorporating the complex slope topography may deviate from the reality in real-world landslide risk assessments. Moreover, the 3D large-deformation analyses enable a more precise estimation of the movement path of the failed mass and its affected area, enhancing the prediction and management of landslide hazards. Overall, a good consistency between the observed and calculated results implies that the CEL model adequately reproduces the affected area of the landslide.

Keywords: Lomba Grande landslide; Volcanic Rock System; Coupled Eulerian-Lagrangian method; Runout dynamics; Faial earthquake.

1. Introduction

The Azores archipelago, located in the Atlantic Ocean and composed of nine volcanic islands as shown in Fig. 1(a), is characterized by unique volcanic rock formations and is frequently impacted by various geohazards and natural disasters, including earthquakes, volcanic eruptions, and extreme meteorological events (Valadão et al., 2002). In seismically active regions such as the Azores, landslides represent a significant threat to infrastructure, human communities, and the environment (Bandara et al., 2016; Guo et al., 2023; Zhao et al., 2023; Cheng et al., 2025; Liu et al., 2025).

One notable seismic event in this region was the Mw 6.2 Faial earthquake on 9 July 1998, which was recorded at a limited number of seismic stations, the closest one located approximately 15 km from the rupturing fault (Oliveira et al., 2008), as shown in Fig. 2. In addition to considerable damage to housing infrastructure, this earthquake triggered a major landslide at Lomba Grande in Figs. 1(b) and (c), near Ribeirinha on Faial Island, as well as multiple rockfalls on São Jorge Island (Fernández et al., 2025). Thus, accurately predicting the complex runout behavior of landslides like the Lomba Grande event during seismic activity (Fig. 2) is crucial for effective risk mitigation and disaster management strategies (Sousa et al., 2014, 2016; Islam et al., 2018; He et al., 2019; Zang et al., 2022).

Traditional small-strain finite element or finite difference methods face significant challenges when modeling landslides involving complex three-dimensional (3D) geometries, spatially heterogeneous materials, and large deformations. These methods often suffer from severe mesh distortion during large deformation processes, resulting in significant numerical errors or even termination due to convergence issues (Chen et al., 2021a; Ren et al., 2023, 2025). Consequently, there is a pressing need to adopt advanced numerical approaches capable of effectively simulating large-scale landslide phenomena.

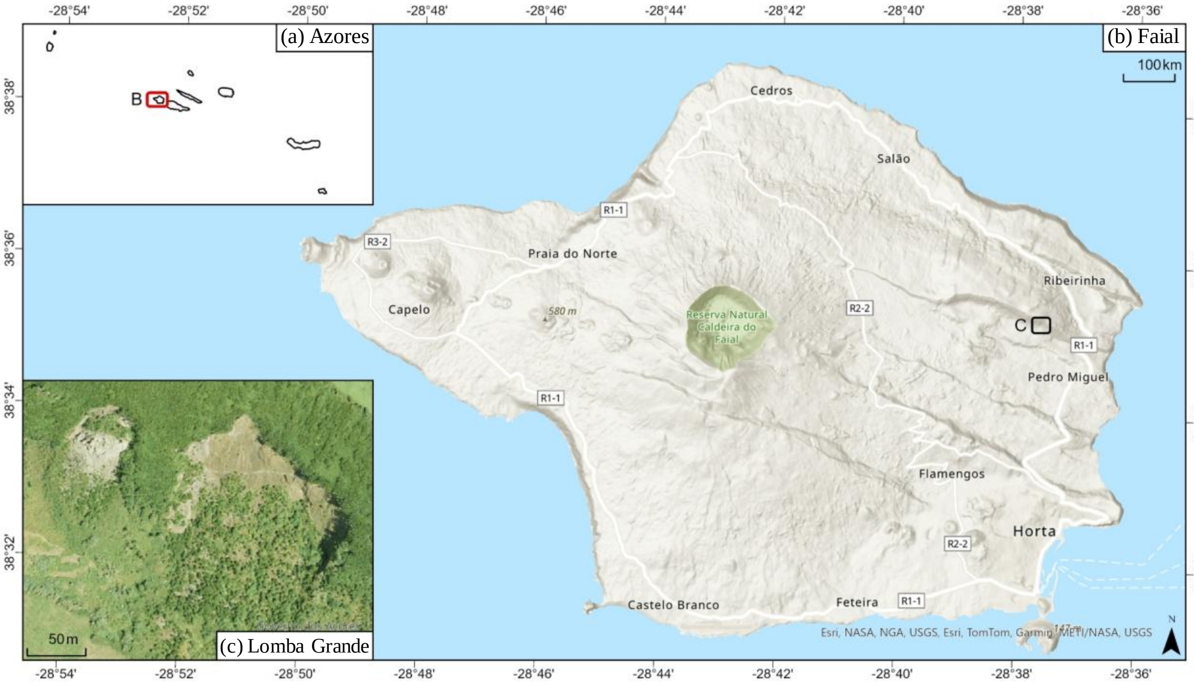

Fig. 1 The Azores Archipelago (a) and the location of Lomba Grande landslide (c) in Faial Island (b).

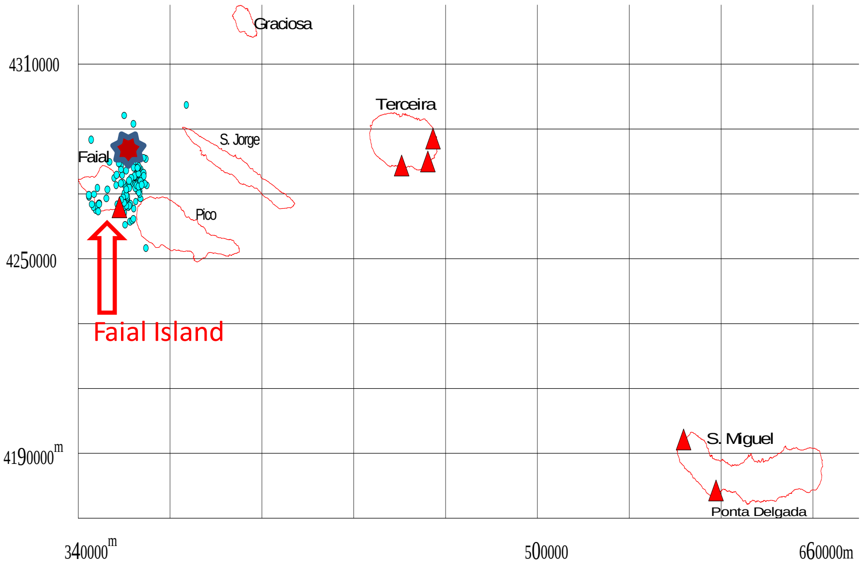

Fig. 2 Epicentral location of the 1998 Faial earthquake (★) and main aftershocks. Red triangles are strong motion stations

In computational mechanics, the motion and deformation of materials are commonly described by Lagrangian or Eulerian frameworks (Noh, 1964). In the Lagrangian method, the motion of materials is tracked by following material points over time, making it suitable for problems in solid mechanics because the evolution of the material variables during deformation can be easily obtained. However, when large deformations occur, computational mesh elements become highly distorted due to the fixed relationship between nodes and material points, and this can produce numerical issues during the numerical integration. In contrast, the Eulerian approach utilizes fixed spatial coordinates, allowing material to flow through the computational mesh. This approach effectively prevents mesh distortion but typically struggles to accurately represent free surfaces and contact interfaces between different materials, and special numerical considerations must be applied to tracking the evolution of material variables depending on the deformation history.

To combine the strengths of both Lagrangian and Eulerian methodologies, researchers have developed advanced large-deformation finite element (LDFE) methods. These methods alternate between Lagrangian and Eulerian analysis steps, thus avoiding severe mesh distortion while accurately capturing free surfaces and material boundaries (Wang et al., 2015). Current mainstream large deformation methods in geotechnical engineering include the Remeshing and Interpolation Technique with Small Strain (RITSS) method (Hu and Randolph, 1998; Liu et al., 2019; Chen et al., 2021b), Coupled Eulerian-Lagrangian (CEL) method (Benson, 1992; Qiu et al., 2011; Chen et al., 2023a, 2023b), Arbitrary Lagrangian-Eulerian (ALE) method (Nazem et al., 2006, 2008), and Hybrid Lagrangian-Eulerian approaches, such as the Material Point Method (MPM) (Liu et al., 2020; Fernández et al., 2021, 2023). Among these, the RITSS method encounters difficulties in capturing free surfaces and interfaces, especially in complex 3D scenarios, while ALE methods often face accuracy deterioration and numerical problems due to mesh quality degradation.

In contrast to RITSS and ALE methods, CEL and MPM effectively address mesh distortion by allowing materials to flow freely within background meshes, enabling simulations of large deformation phenomena such as earthquake-triggered landslides, gravity-driven slope failures, wave-induced landslides, landslide-generated tsunamis, and valley-filling landslides. For example, He et al. (2019) and Li et al. (2020) successfully applied two-dimensional (2D) MPM to model the Daguangbao landslide triggered by the 2008 Wenchuan earthquake in China. Fernández et al. (2024) further extended the 2D analysis to three dimensions, significantly improving the understanding of landslide mechanisms, runout behavior, affected area, and deposition morphology. Similarly, several researchers (Chen et al., 2021a; Liu et al., 2023; Ren et al., 2023) employed CEL-based 2D and 3D large-deformation analyses to model earthquake-induced landslides behavior, such as sliding surfaces, velocity evolution, runout distances, and final deposition patterns. However, most of these studies primarily focused on 2D analyses or 3D analyses with simplified idealized slope geometries, neglecting the complexities of actual topographical conditions.

Therefore, this study aims to reproduce the earthquake-induced Lomba Grande landslide using a 3D CEL large-deformation simulation technique, explicitly incorporating realistic slope geometry. Firstly, the mechanical properties of rock masses at the Lomba Grande site are estimated based on a Volcanic Rock System (VRS) empirical model, and a representative seismic load is derived from records of the Mw 6.2 Faial earthquake. Subsequently, the CEL method is utilized to simulate the runout dynamics, depositional topography, and affected area under seismic conditions. Finally, numerical results are systematically compared against field observations to evaluate the model's predictive capability. This research seeks to provide comprehensive insights into the initiation mechanism, dynamics, and depositional characteristics of earthquake-triggered landslides, emphasizing the effectiveness of the CEL approach in assessing landslide risks in realistic, complex terrains, through a case study.

2. The Lomba Grande landslide

2.1 Background of Lomba Grande landslide

The Azores region is composed of several islands, in which São Miguel, the largest one, is formed by three active volcanoes. These volcanic formations are unique in the sense that they typically exhibit large natural variability of lithological formations and heterogeneities. The central area of São Miguel Island is highlighted by its high seismicity. The first strong motion record on January 1st, 1980 (Oliveira 1992) with the Mw7.2 Terceira earthquake caused a great deal of damage in the building stock and the sloppy areas of São Jorge Island. With the establishment of more stations covering most Islands, the most important event recorded in a few stations was the Mw6.2 Faial earthquake on 9 July 1998 (Oliveira 2008) in Fig. 2. Besides the impact on housing, this earthquake triggered an important landslide (Lomba Grande) in Faial municipality (Faial Island-Azores), as seen in Fig. 1.

Fig. 3(a) depicts the topography map of the Lomba Grande rock slope, obtained from the high-resolution LiDAR topographic data. From a geological point of view, the Lomba Grande slope consists of a rocky mass of a trachytic nature, which is covered superiorly by a deposit of a pyroclastic nature. As shown in Fig. 3(a), the sliding surface (marked as blue lines) and the final deposition (pink lines) are identified by comparing the slope topography from the years 1993 and 2002. Fig. 3(b) depicts a representative landslide profile along section A-A’, which is obtained by stretching line A-A’ using CAD software. The failure surface has a maximum depth of

13.5 m in this section. Significant earthquake-triggered landslide runout is observed. These observed landslide runout characteristics (e.g., sliding surface, runout distance, final deposition profile) can serve as a benchmark for calibrating and validating the subsequent CEL numerical model. By comparing the numerical predictions against these field observations, the accuracy and reliability of the computational approach can be assessed and refined.

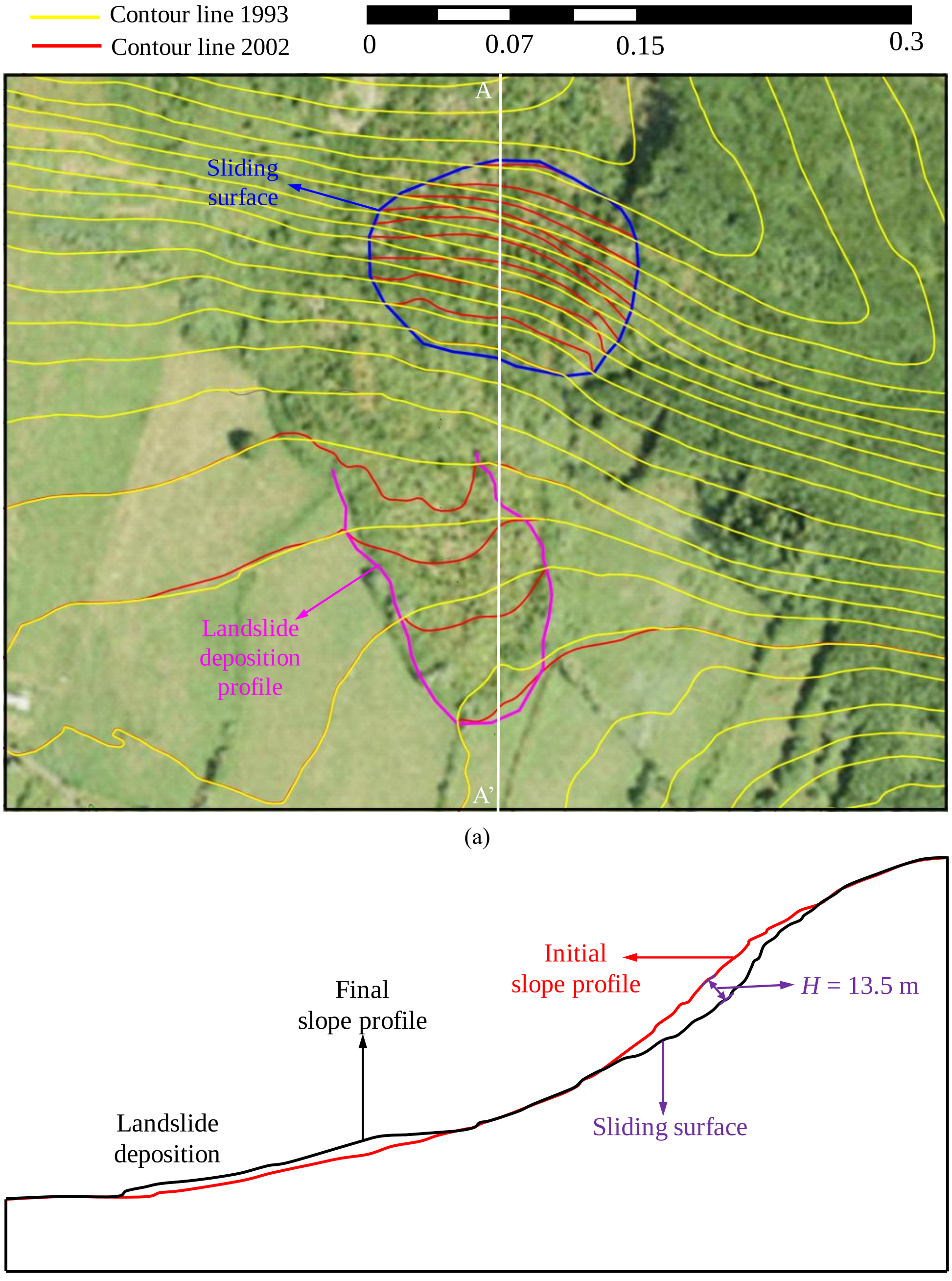

(a)

(b)

Fig. 3 The Lomba Grande landslide: (a) the topography map of Lomba Grande rock slope; (b) the typical landslide section (AA').

2.2 Volcanic rock characterization

The geological formation of the Azores consists primarily of volcanic rocks, shaped by the region's mild, humid Atlantic climate. A distinctive rock type found in the Azores is Andosols, which are almost entirely derived from volcanic rock and composed mainly of explosive debris, such as pyroclastic material and tephra. The volcanic glass within these materials is highly susceptible to chemical weathering, resulting in rapid soil evolution and the formation of amorphous mineral products in the fine soil fraction. This transformation process, often referred to as "archiving", plays a crucial role in the development of Andosols by altering their mineralogical composition and geotechnical properties over time.

A classification system was recently developed for characterizing volcanic rocks, known as the Volcanic Rock System (VRS). The VRS is an adaptation of the widely used Rock Mass Rating (RMR) system (Miranda et al., 2018). This empirical system evaluates volcanic rock masses based on six geological and geotechnical parameters (P_1-Uniaxial compressive strength (UCS), P_2-Rock weathering, P_3-Joint Frequency, P_4-Discontinuity conditions, P_5-Presence of water, P_6-Dosposition of blocks), each assigned relative weights (Miranda et al., 2018; Sousa et al., 2021), as shown in Table 1. The algebraic summation of these six weights results in the final VRS value, with a range of 0 to 100, which can be used for estimating strength properties, deformability moduli, and description of the rock mass quality.

In this study, the VRS empirical system is applied to characterize the rock mass at the Lomba Grande site. The results, summarized in Table 1, indicate that the classification of the pyroclastic rock mass varies between Class VI (Very Poor) and Class V (Poor), with VRS weight values ranging from 17 to 37. The pyroclastic rock exhibits a UCS of lower than 15 MPa and is characterized by highly or extremely weathered condition. Numerous separate and discontinuous joints contribute to the formation of unstable rock blocks, leading to reduced or even unacceptable overall stability. This classification provides a quantitative assessment of the engineering behavior of volcanic rock masses at Lomba Grande, offering valuable insights for numerical modelling by establishing key geomechanical parameters that can be incorporated into computational simulations.

Table 1 Application of VRS to the Lomba Grande landslide

Property	Description	Rock characteristic	VRS rating	Weights
P_1	UCS	UCS < 15 MPa	R5	1
P_2	Rock weathering	Highly or extremely weathered	A3	4
P_3	Joint frequency	11-15 or more per m	F4/F5	5 ~ 10
P_4	Joint surface conditions	Slightly rough discontinuities; Separation >5mm discontinuities	B3/B4	10 ~ 17
P_5	Presence of water	Dry or damp; dripping	C1/C2	7 ~ 10
P_6	Block position	Acceptable to stability; Not acceptable to stability	D3/D4	-10 ~ (-5)
VRS	--	Very Poor to Poor	VI~V	17 ~ 37

Note: Class I (Excellent): VRS = 100-91; Class II (Good): VRS = 90-76; Class III (Reasonable): VRS = 75-61; Class IV (Regular): VRS = 60-41; Class V (Poor): VRS = 40-21; Class IV (Very Poor): VRS = 20-0.

For comparison, the RMR value at the Lomba Grande can be obtained based on the linear correlation between the VRS and RMR coefficients (Miranda et al., 2018):

$$\mathrm{VRS} = 1.06 \times \mathrm{RMR} - 3.134 \tag{1}$$

This gives a RMR value ranging from 19 to 38, corresponding the class V (Very poor) to IV (Poor), which is consistent with VRS classification. However, the VRS system has the advantage to account for the rock weathering effect compared to the empirical RMR system (Miranda et al., 2018).

For the rock mass deformability (Miranda et al., 2018), the relationship obtained for basalts is given by:

$$E = 0.634\mathrm{e}^{0.634\,\mathrm{VRS}} \tag{2}$$

Therefore, for the maximum and minimum values of VRS, the elastic modulus of the pyroclastic rock mass ranges from 2.3 GPa to 3.7 GPa. Given the inherent uncertainties in rock mass behavior, a conservative estimation recommends adopting the lower bound value of 2.3 GPa for pyroclastic rock. The strength parameters of the pyroclastic rock formations are characterized by a friction angle between 30° and 43° and a cohesion ranging from 0 to 9 kPa. Currently, no exact mechanical property data is available for the basalt rock at the site. However, based on existing geological databases, basalt rock typically exhibits an elastic modulus between 10.4 GPa and 38.6 GPa, a friction angle ranging from 59.2° to 66.8°, and a cohesion varying between 0 and 6.27 MPa. These estimated properties provide a reference for numerical modeling and geomechanical assessments of the rock mass at the site.

2.3 The 1998 Faial Earthquake

Earthquakes are a major driver of slope instability in the Azores. Given the region's tectonic activity, a multi-hazard analysis is particularly relevant, as the Azores frequently experience earthquakes, volcanic eruptions, and landslides (Valadão et al., 2002). To account for seismic effects in the analysis, the input ground motion will be applied at the bedrock level, ensuring that the dynamic response of the slope is accurately captured. This allows for a more realistic assessment of earthquake-induced slope instability, incorporating site-specific seismic conditions.

Several procedures can be used to select a set of time series with an increasing value of PGA (peak ground acceleration) and check the degree of non-linearity. The method of work consists of analyzing the most important strong motion records obtained since 1980 and determining their main properties, such as PGA and PGV (peak ground velocity), mean response spectral shape, duration, etc., considering the type of soil formation in each recording station.

Based on the previous discussion, the most suitable seismic record for use in conjunction with the Porto Formoso site is exactly the 1998 record (Mw 6.2) obtained at the station of Horta, Faial (Oliveira 2008). This selection is justified not only because it represents a realistic upper limit of possible seismic action at this site in terms of magnitude and epicentral distance, but also because it aligns closely with the recommendations of both older RSA (1983) guidelines and the more recent NP-EN 1998-1 seismic design code. The main characteristics of the seismic records are summarized in Table 2, following processing with the Seismosoft (2021) program. To eliminate residual velocities and displacements, the earthquake records were subjected to linear baseline correction and filtered using a 4th-order bandpass Butterworth filter within a frequency range of 0.2 to 20 Hz. When compared to the 1998 Faial earthquake signal used in the Porto Formoso landslide (Fernández et al., 2025), the intensity of the ground motion in this study is amplified by 1.5 to correctly represent the effect of the earthquake at the Lomba Grande site, which is half way between the epicentral area and the station recording the event (Horta).

Fig. 4 presents all three components (acceleration, velocity, and displacement) of the earthquake in the X, Y, and Z directions. As observed, the corrected signals return to approximately zero levels at the end of the motion duration. The total ground motion duration is 9.34 seconds, representing the most intense phase of shaking. This earthquake exhibits high intensity, with maximum accelerations of 6.45 m/s², 6.26 m/s², and 4.51 m/s² in the X, Y, and Z directions, respectively. These values indicate a strong shaking event, which is essential for evaluating the seismic response of the studied site.

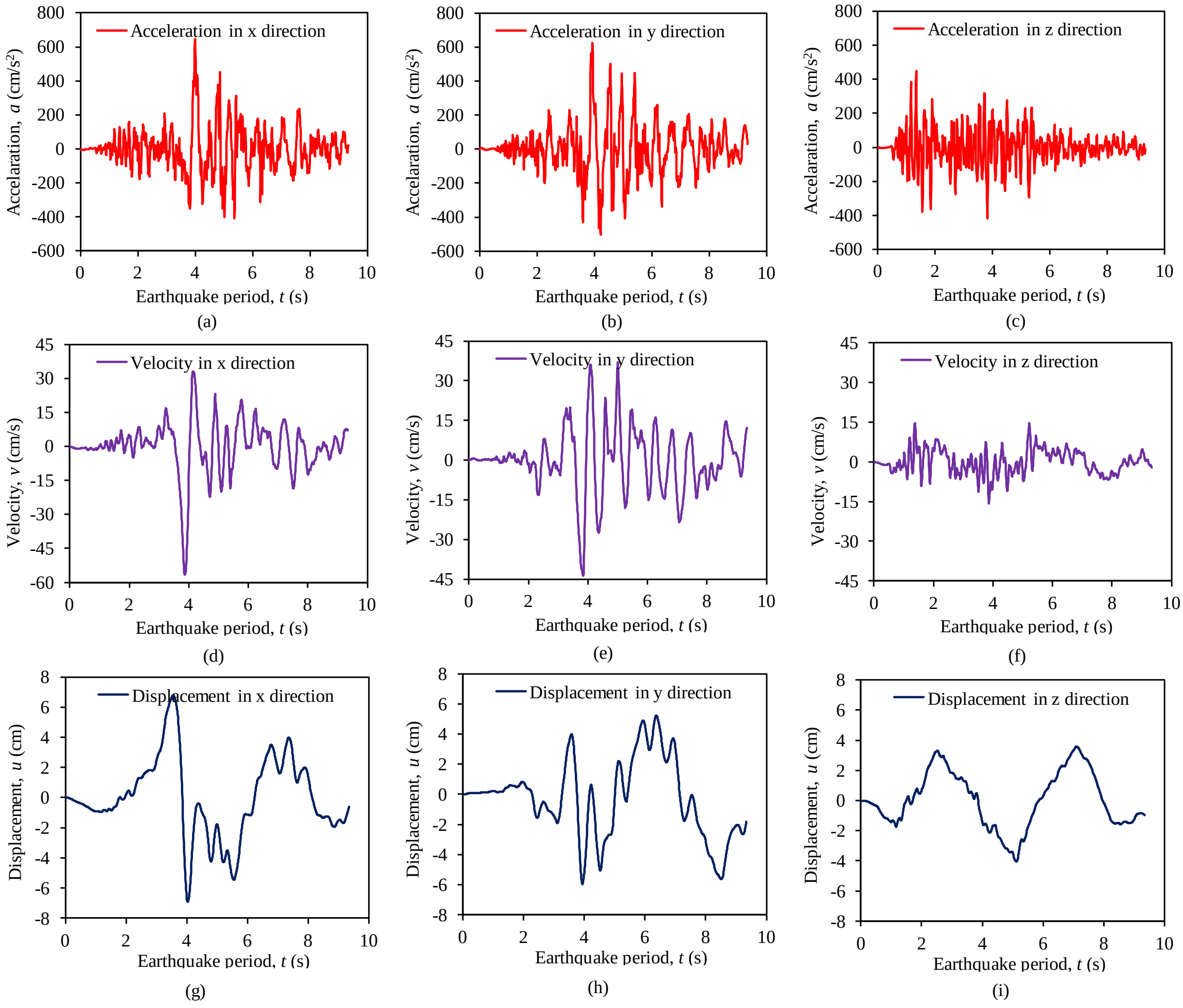

Fig. 4 Earthquake signals applied at the base rock in the numerical modeling

Table 2 Peak values of each component for the Faial Earthquake in all three directions

Parameter	X-direction	Y-direction	Z-direction(vertical)
Maximum acceleration (cm/s^2)	645.23	625.67	450.90
Moment of maximum acceleration (s)	3.99	3.93	1.34
Maximum velocity (cm/s)	56.61	36.93	15.69
Moment of maximum velocity (s)	3.86	3.84	3.86
Maximum displacement (cm)	6.91	5.97	4.04
Moment of maximum displacement (s)	4.03	3.94	5.12
Earthquake period (s)	9.34	9.34	9.34

3. Framework of numerical methods

3.1 CEL-LDFE approach

The CEL method combines the Eulerian and Lagrangian methods for modeling large deformation processes without issues related to mesh distortion (Benson, 1992; Benson and Okazawa, 2004). In CEL, the deformed and undeformed bodies are modeled by Eulerian and Lagrangian materials, respectively. Eulerian materials are allowed to flow in the Euler background meshes freely. Unlike traditional methods, the CEL approach can maintain accuracy and prevent computational termination due to mesh distortion, even under conditions of extremely large deformation of materials. The governing equation in CEL is defined as Eq. (3):

$$\frac{\partial f}{\partial t} + \nabla \cdot \psi = S \tag{3}$$

where f denotes the variables, ψ represents the flux function and S is the source term. Using the operator splitting technique, the solving process of Eq. (3) can be divided into two sequential steps, namely the Lagrangian step (Eq. (4)) and the Eulerian step (Eq. (5)), respectively (Benson, 1992; Benson and Okazawa, 2004).

$$\frac{\partial f}{\partial t} = S \tag{4}$$

$$\frac{\partial f}{\partial t} + \nabla \cdot \psi = 0 \tag{5}$$

Eq. (4) is identical to the standard Lagrangian formulation. The momentum conservation is expressed in the form of virtual work quation, as

$$\begin{aligned} &\int_{\Omega} \rho a_i \delta u_i \mathrm{d}V + \int_{\Omega} \sigma_{ij} \delta u_{i,j} \mathrm{d}V - \\ &\int_{\Omega} \rho b_i \delta u_i \mathrm{d}V - \int_{\Gamma} t_i \delta u_i \mathrm{d}V = 0 \end{aligned} \tag{6}$$

where δu_i is virtual displacement, a_i is the spatial acceleration, and t_i is an external traction on the boundary Γ. The discrete equation is

$$Ma + F^{\mathrm{int}} = F^{\mathrm{ext}} \tag{7}$$

where M is the mass matrix, F^{int} and F^{ext} are the internal and external force vectors, respectively. The central difference method is used to advance the solution in time with the explicit formulation.

$$\begin{aligned} &a = M^{-1} + \left(F^{\mathrm{ext}} - F^{\mathrm{int}}\right) \\ &v^{n+1/2} = v^{n-1/2} + \Delta t \cdot a \\ &u^{n+1/2} = u^{n-1/2} + \Delta t \cdot v^{n+1/2} \end{aligned} \tag{8}$$

Material interfaces and free surfaces are identified by the Eulerian Volume Fraction (EVF) within each element. The EVF ranges between 0 and 1. When a Eulerian cell is completely filled with material, its EVF is 1; when it contains no material, its EVF is 0. If the EVF of a Eulerian cell is greater than 0 but less than 1, the cell is partially filled with material. Therefore, within each time increment step, it is necessary to recalculate the EVF of each Eulerian material in each cell and use this data to reconstruct the boundaries of each Eulerian material. The range of the Eulerian computational domain generally exceeds the material boundaries to ensure that all material movements and deformations are contained within the Eulerian domain. If the Eulerian material extends beyond the boundaries of the Eulerian computational domain, it will no longer be included in subsequent calculations. As seen in Fig. 5, it is assumed in CEL that the Eulerian mesh nodes bond with the Eulerian materials in the Lagrangian time step, which leads to the deformation of Eulerian elements with the motion of the Eulerian material. In the following Eulerian time step, the deformation of the Eulerian material is terminated, and the deformed Eulerian mesh is recovered to its initial state with all solution variables being mapped from the deformed meshes onto the background meshes (Dassault Systémes, 2018). The CEL approach has been proven effective and efficient in modeling the large-deformation landslide runout by Chen et al. (2021, 2025) and Ren et al. (2023).

The CEL method has been embedded in the commercial finite element software ABAQUS (Dassault Systèmes, 2018). The interaction between Euler and Lagrange bodies relies on the general contact algorithm built in ABAQUS software (Dassault Systémes, 2018). As shown in Fig. 6, key nodes are designated at Lagrangian element boundaries with corresponding anchor nodes on Eulerian surfaces. At the start of each step, the system assesses the displacement (Δx) of anchor nodes penetrating the Lagrangian boundary. A normal contact force (σ_i), inversely proportional to Δx and dictated by the penalty stiffness coefficient (k_i), is then applied:

$$\sigma_i = -k_i \Delta x \tag{9}$$

The tangential contact force is computed by the Coulomb friction with an assigned friction factor at the interface.

$$\tau_i = \mu \sigma_i \tag{10}$$

The automatic step time is applied in CEL during the calculation to minimize computing time and enhance accuracy. The computational stability of the CEL model hinges on a critical incremental step (Δt_{crit}), which is a function of the element size (L_e) and the velocity of material waves (c_d), as delineated in Eq. (11):

$$\Delta t_{\text{crit}} = L_e / c_d \tag{11}$$

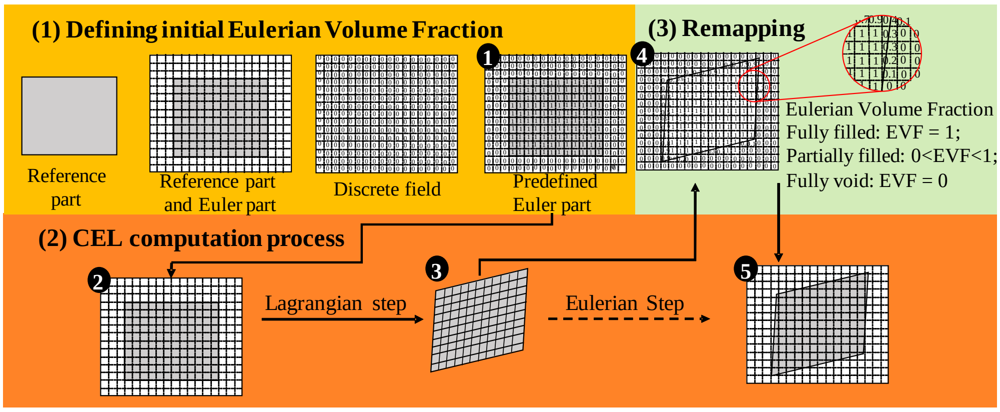

Fig. 5 Definition of EVF and calculation procedure in CEL

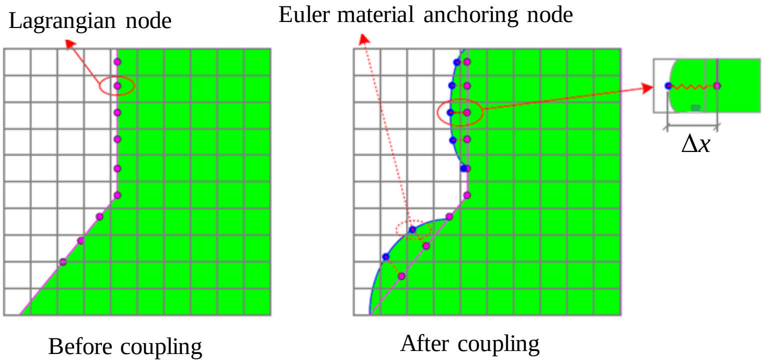

Fig. 6 Interaction between Lagrangian and Eulerian bodies in CEL (Dassault Systèmes, 2018)

3.2 Numerical discretization of slope

Constructing the 3D slope model with real geometry is a complex process in CEL. It involves generating a 3D solid body and defining a Eulerian volume fraction (EVF) using the Discrete Field method in Abaqus. The EVF is then applied to fill the slope geometry in CEL. A detailed description of the model discretization for CEL is imperative.

In the CEL model, the 3D geometry and mesh partitioning of the Lomba Grande rock slope are illustrated in Fig. 7. To capture the landslide runout process accurately, the slope failure surface is explicitly modeled. The model consists of three key components: a rectangular Eulerian domain, a base rock slope with actual geometry, and a failed rock mass. Developing a CEL-based large-deformation finite element model is a complex procedure that involves the following four steps:

(1) **3D base rock slope model generation:** The 3D base rock slope (Fig. 7) is created using SolidWorks based on the topography map of the 1993 Lomba Grande rock slope (Fig. 3a). The 2D topography contour line is extended vertically and interpolated horizontally to generate a 3D base rock slope model with dimensions of 466 m (length), 308 m (width), and 190 m (height). The 3D rock slope model is then imported into Abaqus 2018 and meshed using Lagrangian elements.

(2) **Eulerian domain construction:** A rectangular Eulerian domain is created in Abaqus with dimensions of 466 m × 308 m × 230 m, ensuring it fully encompasses the foundation rock slope to minimize boundary effects during the landslide runout simulation. The Eulerian domain is discretized using 3D 8-node Eulerian elements with reduced integration (EC3D8R), with a minimum mesh size of 2.0 m, resulting in 4,126,430 elements. This mesh configuration achieves an optimal balance between computational cost and numerical accuracy.

(3) Identification of the sliding surface: The sliding surface is identified by comparing the pre-landslide and post-landslide topographic maps. The failed mass is extracted by cutting the 3D base rock slope along the sliding surface.

(4) EVF definition: The Discrete Field method in Abaqus defines the EVF. The Eulerian elements occupied by the failed mass are assigned EVF = 1.0, indicating they are filled with material. In contrast, the remaining elements are treated as voids, allowing the failed mass to move freely during the landslide runout.

It should be noted that only the failed mass is modeled as Eulerian material due to its large-deformation behavior during the landslide runout. The base rock slope is defined as Lagrangian material using 3D tetrahedral elements, as it experiences small deformations under earthquake loading. The Lagrangian elements can overlap the void Eulerian background elements until they encounter Eulerian elements containing Eulerian materials (i.e., the failed mass). The contact between the Lagrangian and Eulerian elements in CEL is governed by the general penalty function contact method. This setup ensures that the CEL-based model effectively captures failure initiation, runout dynamics, and deposition processes, providing a realistic simulation of the Lomba Grande landslide. The CEL simulation was performed using 54 threads on a high-performance Dell workstation equipped with an Intel Xeon W7-3465X CPU, 192 GB of RAM, and running a Windows operating system. The complete analysis of the 71-second landslide runout event requires approximately 22 hours of computation.

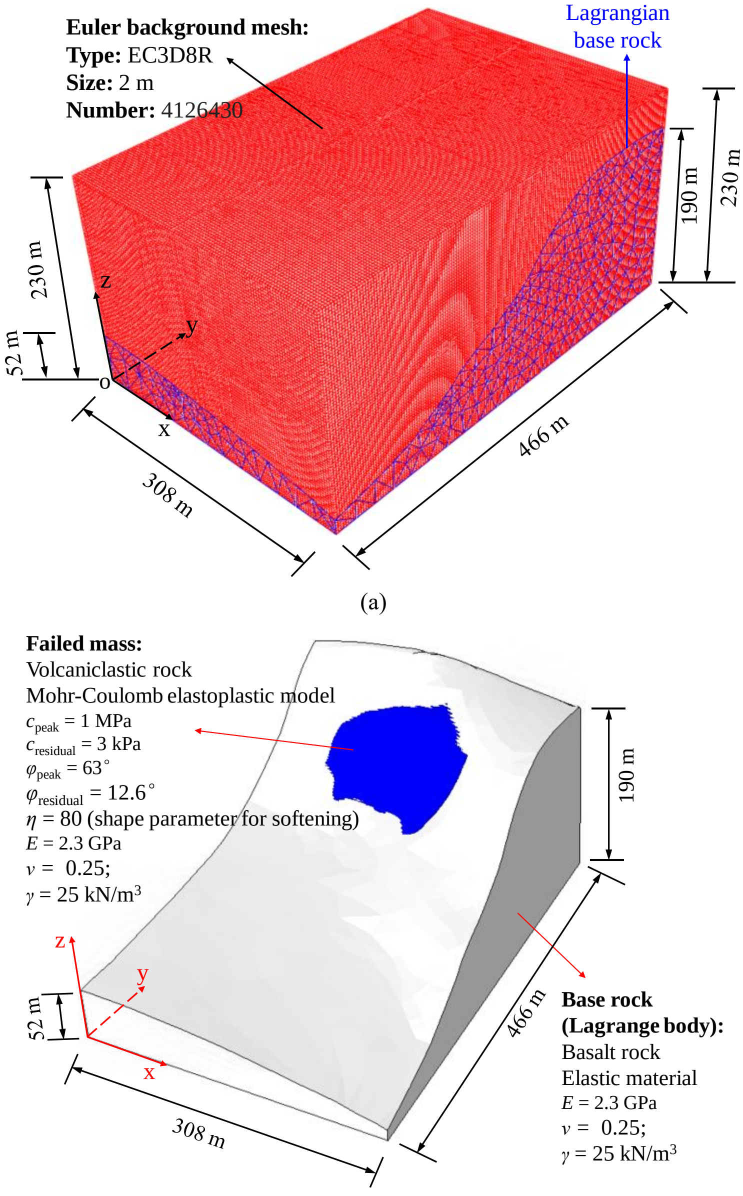

(a)

(b)

Fig. 7 Geometric dimensions and mesh partition of the 3D Lamba Grande slope model in CEL: (a) 3D computational domain with meshes; (b) 3D rock slope model without meshes.

3.3 Rock constitutive model

The study employs distinct rock constitutive models for the base rock and the failed mass to accurately simulate the landslide runout process. The parameters governing these models are outlined below. The base rock mainly consists of Basalt rock, which is modeled using elastic materials owing to the small deformation during the earthquake-triggered landslide runout process. The Young's modulus and Poisson's ratio of the base rock are 2.3 GPa and 0.25. These values reasonably range within the probable limits of the Basalt rock, reported in section 2.1.

The failed mass is made up of volcaniclastic rock, which is represented by the Mohr-Coulomb elastic-plastic constitutive model to capture the post-failure dynamics, with mechanical parameters listed in Table 3. The failed mass has a dilation angle (ψ) of 0°, a unit weight (γ) of 25 kN/m^3 and an elastic modulus (E) of 2.3 GPa, and a Poisson's ratio (v) of 0.25. During the runout, the failed mass undergoes significant strength reduction due to strain-softening effects (Fernández et al., 2024, 2025). The peak and residual cohesions (c) are set at 1.0 MPa and 3 kPa, while the peak and residual friction angles (φ) are 63° and 12.6°, respectively. To account for softening effects caused by the accumulation of effective plastic strain, Fig. 8 presents an exponential model applied in both CEL, expressed as:

$$\begin{aligned} \varphi &= \varphi^{r} + \left(\varphi^{p} - \varphi^{r}\right) e^{-\eta\varepsilon} \\ c &= c^{r} + \left(c^{p} - c^{r}\right) e^{-\eta\varepsilon} \end{aligned} \tag{9}$$

where η is a shape parameter that controls the rate of the strength reduction; ε is the effective plastic strain of the rock, calculated by

$$\varepsilon = \sqrt{\frac{2}{3}\left[\left(\varepsilon_{11}^{p}\right)^{2} + \left(\varepsilon_{22}^{p}\right)^{2} + \left(\varepsilon_{33}^{p}\right)^{2} + 2\left(\varepsilon_{12}^{p}\right)^{2} + 2\left(\varepsilon_{13}^{p}\right)^{2} 2\left(\varepsilon_{23}^{p}\right)^{2}\right]} \tag{10}$$

Both cohesion and friction angle are reduced with a same shape factor (η) of 80. Notably, the residual friction angle, residual cohesion, and shape factor have been carefully calibrated by best fitting field deposition profiles.

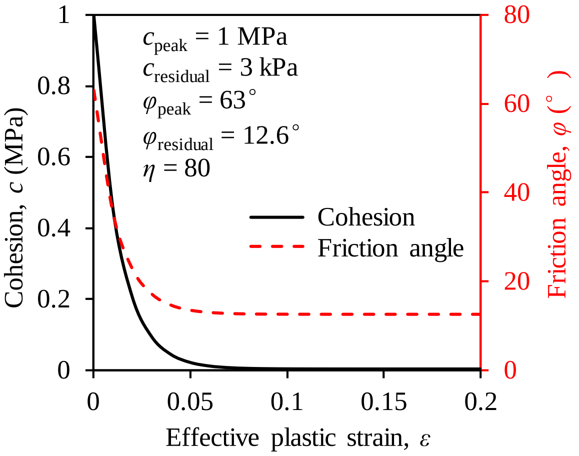

Fig. 8 The exponential softening model used in CEL

Table 3 Parameters for the base slope and failed mass in the CEL model

Parameter	Symbol	Unit	Value
(a) Failed mass (Volcaniclastic rock)			
Peak friction angle	φ_{p}	°	63
Peak cohesion	c_{p}	MPa	1.0
Residual friction angle	Φ_{r}	°	12.6
Residual cohesion	c_{r}	kPa	3
Shape parameter for softening model	η	--	80
Dilation angle	ψ	°	0
Young's modulus	E	GPa	2.3
Poisson's ratio	v	--	0.25
Unit weight	γ	kN/m^3	25
(b) Base rock slope (Basalt rock)			
Young's modulus	E	GPa	2.3
Poisson's ratio	v	--	0.25
Unit weight	γ	kN/m^3	25

3.4 Boundary and load conditions

For earthquake-triggered landslide modeling, boundary conditions are exerted in three steps: geostatic step, earthquake step, and free-sliding step. For the geostatic step, the constraints are applied at the boundaries of the Eulerian domain with the normal constraint at the four side faces and three-direction constraints at the bottom face. This setup aims to prevent material points from flowing out of the Eulerian domain in CEL. Only vertical displacements of the side faces are allowed to achieve the stress balance in the geostatic step.

In the geostatic step, the interface between the base rock and the failed mass is considered as a friction contact with a Coulomb friction factor of 0.7, which is determined by couple of trials to find out the minimum value to maintain slope stability under gravity. This approach has been widely adopted in the landslide runout modeling by previous research (e.g., Fernández et al., 2024)

In the earthquake step, the constraints at the bottom face of the base rock are released. Instead, the earthquake loads in Fig. 2 are applied at the bottom face in three directions to trigger the landslide with an active time of 9.34 s in the CEL model. To minimize the influence of wave reflection under dynamic loading, non-reflecting boundaries (Islam et al., 2018; Fernández et al., 2024) are exerted on the four side faces of the Eulerian domain to dissipate the radiant energy.

In free-sliding step, the earthquake loading is terminated, and the slope continues the runout process driven by both gravity and inertial force for a short time until the movement is halted by the friction between the failed mass and the base rock.

4. Results and discussion

This section presents the modeling results based on the CEL. The runout process, velocity evolution, and plastic strain development during the landslide are analyzed in detail. Additionally, the sliding surface, deposition topography, and affected area by the landslide are compared with the observed information, which can serve as a benchmark for evaluating the numerical model's performance.

4.1 Landslide runout process

The CEL-LDFE analysis is conducted as a preliminary step to provide insights into the runout behavior of the Lomba Grande landslide. Fig. 9 depicts the evolution process of the velocity field from the initial activation to the final termination of the landslide. To analyze the evolution process in detail, two monitoring points are selected: P_1 (143.69 m, 366.88 m, 152.34 m) and P_2 (197.57 m, 345.83 m, 149.35 m), using the trace particle method in Abaqus. Fig. 10 presents the development of the kinetic energy, plastic dissipation energy, and frictional dissipation energy of the failed mass during the landslide. The whole runout process can be distinctly categorized into six stages:

(1) **Geo-stress balance stage (*t* = 0–1 s):** Before applying the earthquake loading, the geo-stress balance is achieved by applying gravity onto the soil at $t = 0$–1 s. During this stage, the failed mass can maintain its stability by the frictional interaction with base rock to counteracts the gravity, as shown in Fig. 9(a).

(2) **Activation stage (*t* = 1–7.54 s):** The earthquake is applied at the base of the base rock between $t = 1$–10.34 s. Initially, the failed mass remains stable due to low-intensity seismic excitation during $t = 1$–3 s, as indicated by the absence of kinetic energy and velocity in Fig. 10. However, following significant ground motion between t = 3–5.86 s, the failed mass loses stability, as depicted in Fig. 9(b), and a sliding surface develops at the interface between the failed mass and the base rock. By $t = 5.9$ s, the maximum velocity of the rock within the failed mass reaches 1.2 m/s, while the kinetic energy begins to rise sharply, marking the activation of slope failure.

(3) **First accelerating stage (*t* = 7.54–10.34 s):** The combined driving forces of earthquake shaking and gravity exceed the frictional resistance, resulting in rapid acceleration of the landslide from the maximum sliding velocity ($V_{\max}$) of 1.2 m/s to 23.3 m/s. At this stage, the failed mass retains its initial geometry with minimal deformation.

(4) **Second acceleration stage (*t* = 10.34–14.54 s):** After $t =$ 10.34 s, the ground motion ceases. However, due to the relatively small contact area between the failed mass and the basal rock, frictional resistance remains lower than the driving force, allowing the landslide to continue accelerating under gravity and inertial effects. By $t =$ 14.54 s, the failed mass reaches its maximum velocity of 46.1 m/s, corresponding to the peak kinetic energy, as indicated in Fig. 10. During this stage, large deformations occur, and the landslide undergoes extensive runout.

(5) **Deceleration stage (*t* = 14.54–50 s):** After $t = 14.54$ s, the increasing contact area between the failed mass and the basal rock results in greater frictional resistance, which eventually exceeds the driving forces from gravity and inertia. Consequently, the velocity gradually declines from 46.1 m/s to 0 m/s. By $t = 50$ s, kinetic energy and sliding velocity approach zero in Fig. 10, signifying the end of the landslide runout process.

(6) **Stabilized stage (*t* = 50–70 s):** After $t = 50$ s, the deformed soil slope stabilizes under gravity with zero kinetic energy and velocity, indicating the complete termination of the landslide movement.

The numerical results confirm that the Lomba Grande landslide is a high-energy geo-disaster characterized by extremely rapid movement of the failed mass. The landslide dynamics pose a significant threat to surrounding lives and infrastructure. Neglecting these dynamics in numerical modeling tends to result in an underestimation of the associated disaster risk.

During the runout phase ($t = 5.86$–50 s), frictional interactions between the failed mass and the base rock generate substantial plastic strain in the failed mass. As shown in Fig. 11, the plastic strain initially develops in the area in contact with the base rock and then in the upper region of the failed mass. The highest plastic strain values typically develop along the interface between the failed mass and the underlying base rock. As the landslide mass moves downslope, plastic strains accumulate within the rock, resulting in significant dissipation of plastic strain energy, as illustrated in Fig. 10. Neglecting this plastic energy dissipation in numerical models may lead to an overestimation of landslide runout distances and impact forces. Such inaccuracies could result in improper hazard zoning and unnecessarily conservative design of mitigation measures, underscoring the critical importance of accurately accounting for plastic energy dissipation in landslide simulations. Additionally, frictional work between the failed mass and the basal rock represents another energy dissipation mechanism during landslide runout. This highlights the necessity of accurately simulating the interaction between the failed mass and the base rock to account for frictional dissipation and predict long-runout behavior correctly. However, it should be noted that plastic dissipation still dominates energy loss during the landslide compared to frictional dissipation, as shown in Fig. 10. The dominance of plastic dissipation may be attributed to the fact that it occurs throughout the entire failed mass. In contrast, frictional dissipation is restricted to the interfaces between the failed mass and the bedrock.

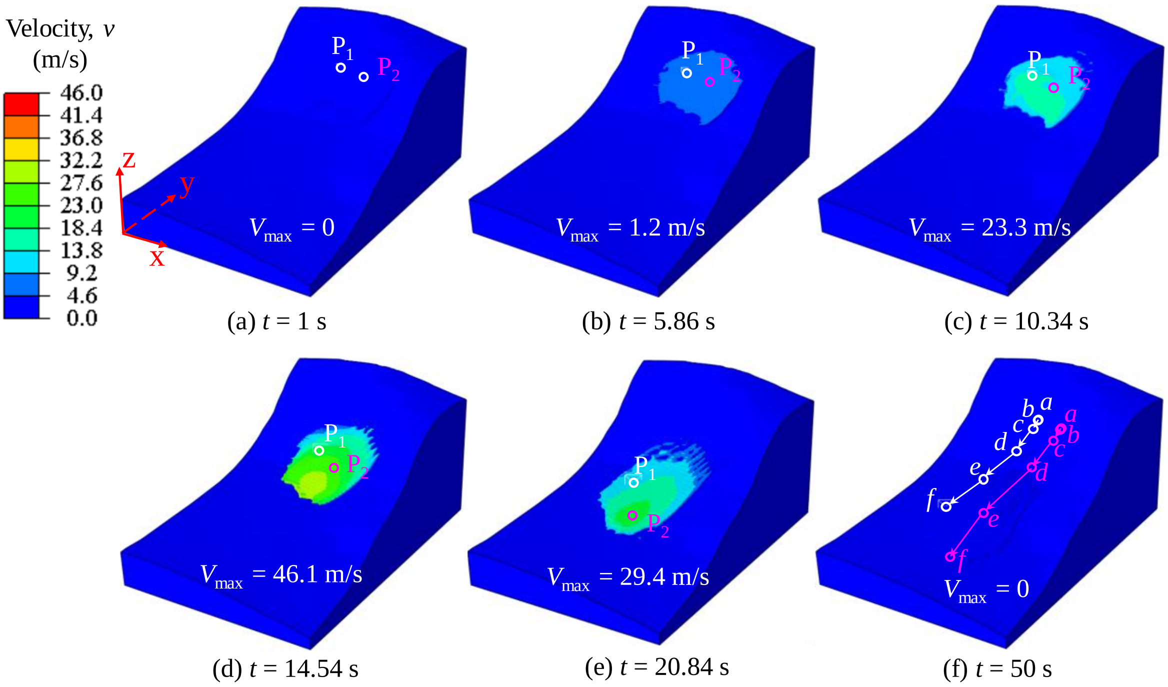

(a) t = 1 s (b) t = 5.86 s (c) t = 10.34 s

(d) t = 14.54 s (e) t = 20.84 s (f) t = 50 s

Fig. 9 Evolution of sliding velocity for the Lomba Grande landslide.

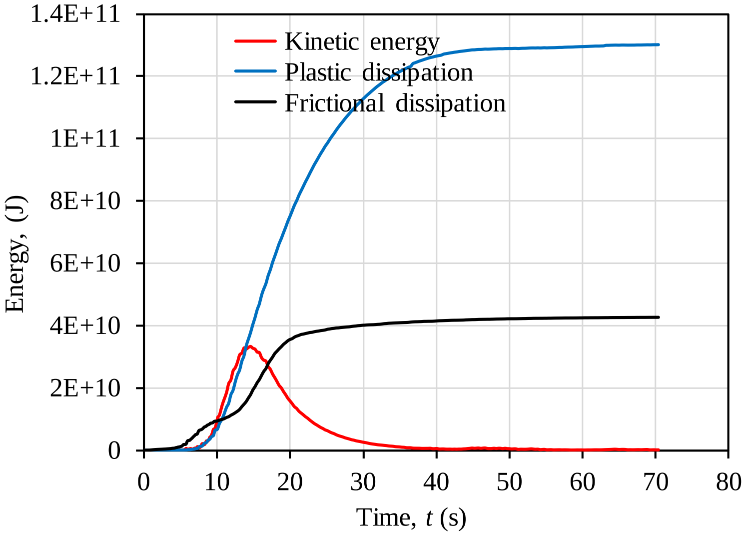

Fig. 10 Evolution of kinetic energy, plastic dissipation energy and frictional dissipation energy of the failed mass.

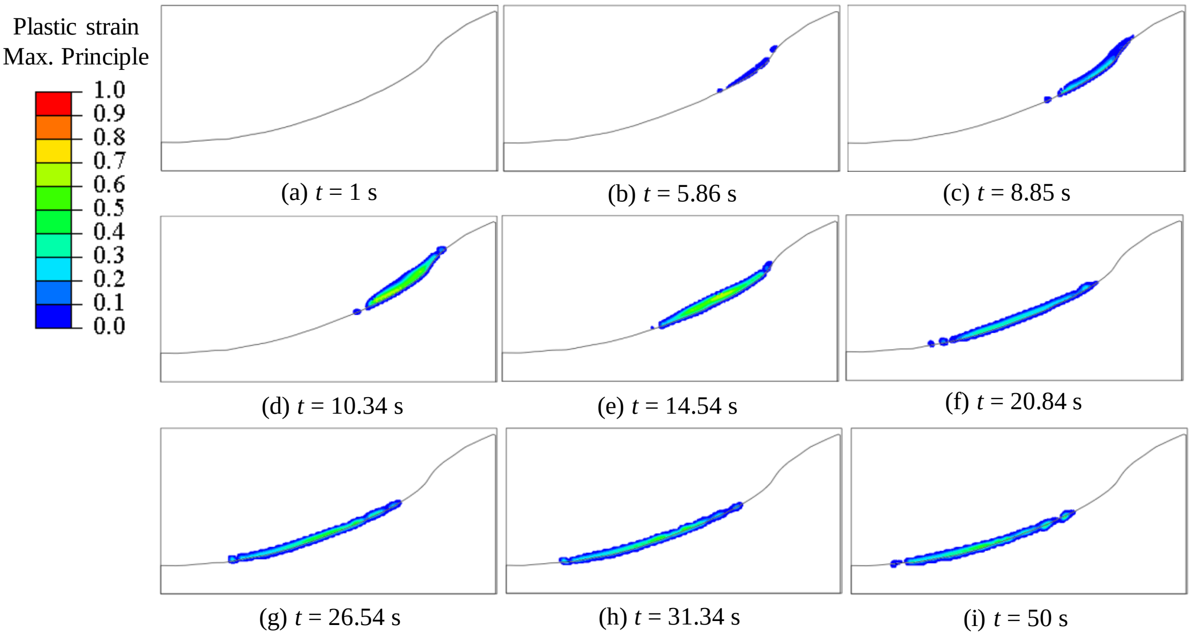

(a) *t* = 1 s (b) *t* = 5.86 s (c) *t* = 8.85 s (d) *t* = 10.34 s (e) *t* = 14.54 s (f) *t* = 20.84 s (g) *t* = 26.54 s (h) *t* = 31.34 s (i) *t* = 50 s

Fig. 11 Evolution of the plastic strain (maximum principle) of a 2D slope section for the Lomba Grande landslide.

Figs. 12(a) and (b) recorded the monitored velocities in all three directions at the selected monitored points P_1 and P_2, respectively. The velocity evolution at both points indicates that the Lomba Grande landslide exhibits the highest velocity in the Y direction and the lowest in the X direction. This observation is mainly attributed to the slope topography, leading to relatively larger gravitational force components along the slope direction (Y-direction) than the lateral direction (X-direction). Compared to the velocity evolution at point P_1, point P_2 experiences a different movement pattern, characterized initially by velocity in the negative X-direction, followed by movement in the positive X-direction. This indicates that the failed mass first shifts toward the left side and subsequently moves toward the right side of the base rock, primarily due to the influence of the local topography. This phenomenon is further confirmed by examining the evolution of velocity vectors of the failed mass depicted in Fig. 13. Such observations underscore real-world landslides are significantly influenced by complex slope topography. Consequently, without capturing realistic topographical details, the simplified assumption of an idealized slope may lead to predictions that deviate considerably from reality. This highlights the importance of incorporating detailed, real-world topography in landslide risk assessments, particularly in regions highly susceptible to slope failures.

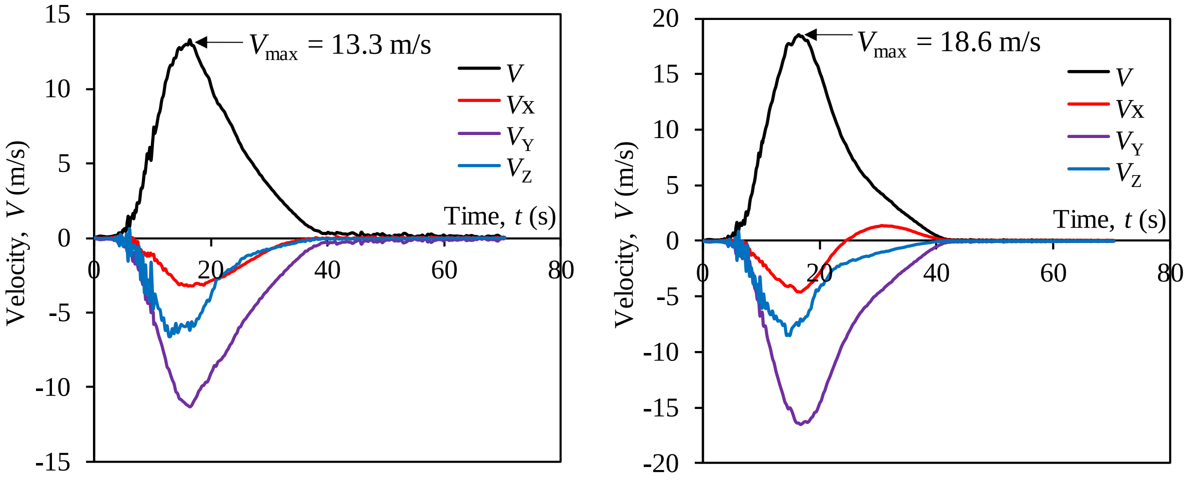

(a) (b)

Fig. 12 Velocity evolution of the reference points P_1 and P_2: **(a)** P_1(143.69 m, 366.88 m, 152.34 m); **(b)** P_2(197.57 m, 345.83 m, 149.35 m).

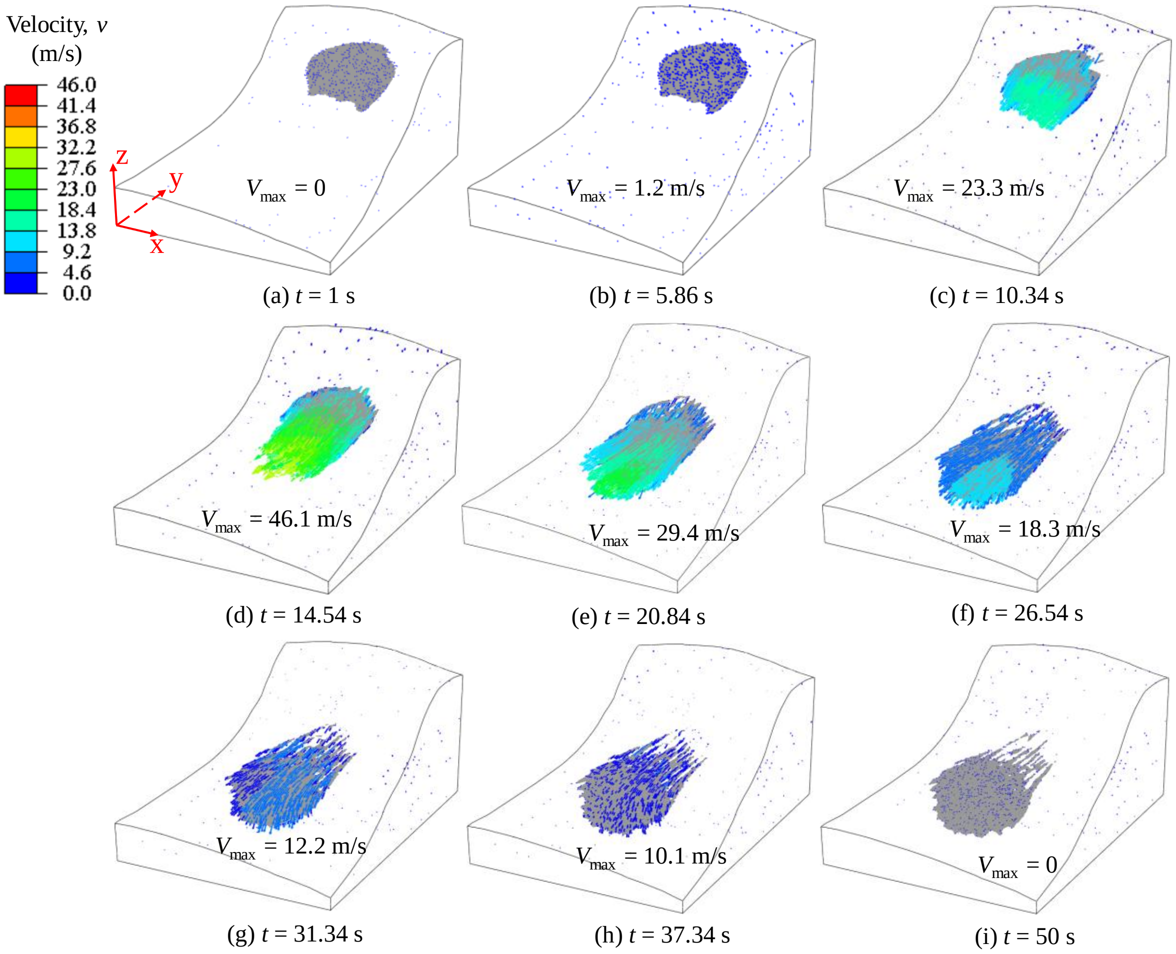

(a) t = 1 s (b) t = 5.86 s (c) t = 10.34 s

(d) t = 14.54 s (e) t = 20.84 s (f) t = 26.54 s

(g) t = 31.34 s (h) t = 37.34 s (i) t = 50 s

Fig. 13 Evolution of velocity vector for the Lomba Grande landslide.

4.2 Final deposition topography

Fig. 14 shows the position evolution of the failed mass during the landslide runout for a typical 2D slope section. The initial sliding surface in Fig. 14(b) is consistent with the predefined failure surface. The runout distance in the horizontal direction can be defined as the displacement of the slope toe of the failed mass, as shown in Figs. 14(c-f). During the earthquake (t = 1-10.34 s), the failed mass has a horizontal runout distance of 6 m, while a larger runout distance of 207.5 m is observed in the free-sliding step (t = 10.34-50 s). This is attributed to the highest kinetic energy at the free-sliding stage, induing a great inertia effect, as indicated in Fig. 10.

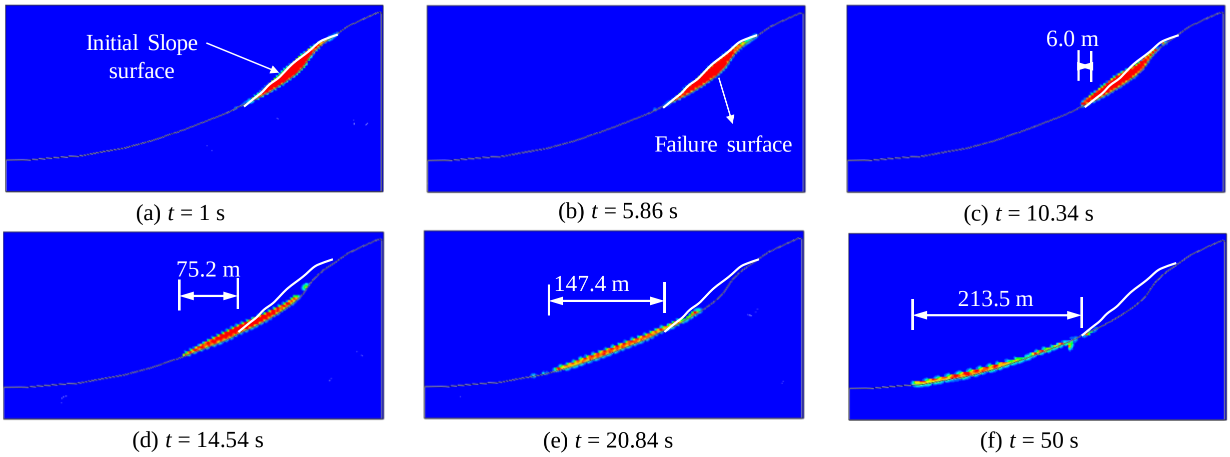

(a) t = 1 s (b) t = 5.86 s (c) t = 10.34 s

(d) t = 14.54 s (e) t = 20.84 s (f) t = 50 s

Fig. 14 Evolution of the failed mass of a 2D slope section for the Lomba Grande landslide.

Fig. 15 compares the initial and final landslide profile obtained from the numerical modeling and the observed topography in Fig. 3(b). Overall, the numerical results exhibit strong agreement with the field observations in the 2D slope section, capturing key characteristics such as the initial slope geometry, the failure surface, and the final deposition profile. The similarity between the simulated and observed profiles suggests that the numerical model effectively reproduces the primary deformation mechanisms and the extent of material displacement. This alignment highlights the model's capability to accurately simulate the landslide process, providing confidence in its ability to predict slope failure behavior under similar geological and loading conditions.

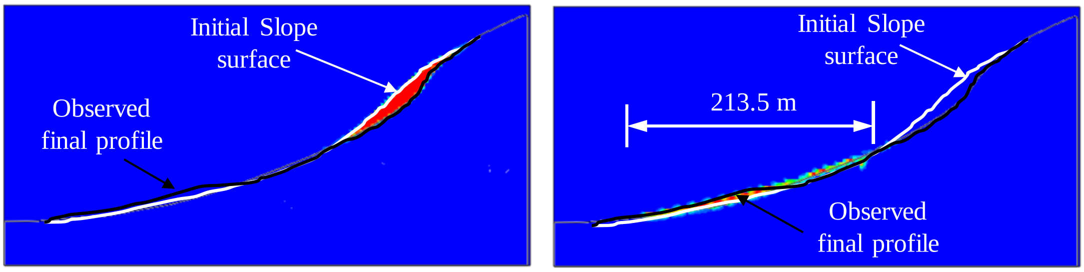

(a) (b)

Fig. 15 Comparison of the landslide profile with the observed topography: (a) before the landslide; (b) after the landslide.

4.3 Affected area

CEL-LDFE modeling in three dimensions enables estimating the movement process of the failed mass and the affected area on the base rock. Fig. 16 displays the evolution of the deposition topography of the failed mass during the landslide. The failed mass runs forward for a long distance, with a final deposition in Fig. 16(f).

As shown in Fig. 16(a), the reference points P_1 and P_2 within the failed mass are set in CEL model to capture the landslide runout process, with the final trajectory in Fig. 16(f). Fig. 17 illustrates the displacement evolution of the reference points. The point P_1 shows a final displacement of 212.2 m, comprising -52.5 m in the X direction, -187.7 m in the Y direction, and -83.8 m in the Z direction. In comparison, P_2 shows a more significant displacement of 284.8 m, comprising -31.7 m in the X direction, -263.6 m in the Y direction, and -103.0 m in the Z direction. Fig. 18 compares the final deposition topography in a plane view between the field observation and the numerical calculation. While the simulated affected area does not perfectly match the observed one in terms of geometry, the overall extent is largely consistent. This general agreement between the observed and calculated deposition zones indicates that the CEL model effectively captures the deposition profile.

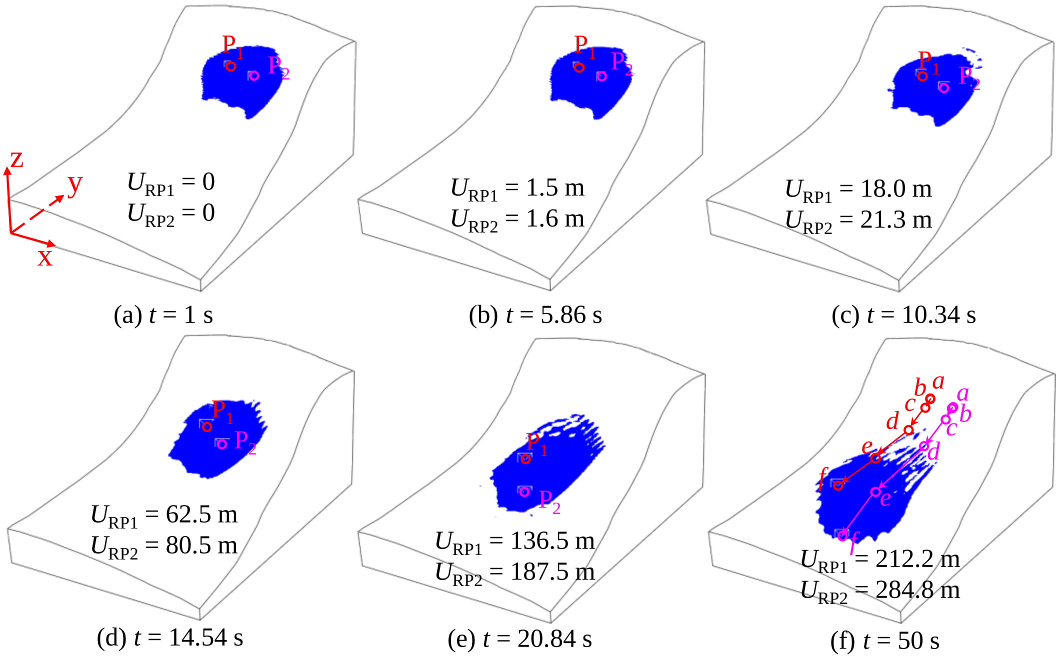

(a) t = 1 s (b) t = 5.86 s (c) t = 10.34 s

(d) t = 14.54 s (e) t = 20.84 s (f) t = 50 s

Fig. 16 Evolution of deposition topography for the Lomba Grande landslide (U_{RP1} and U_{RP2} represents the total displacement of the reference points P_1 and P_2, respectively).

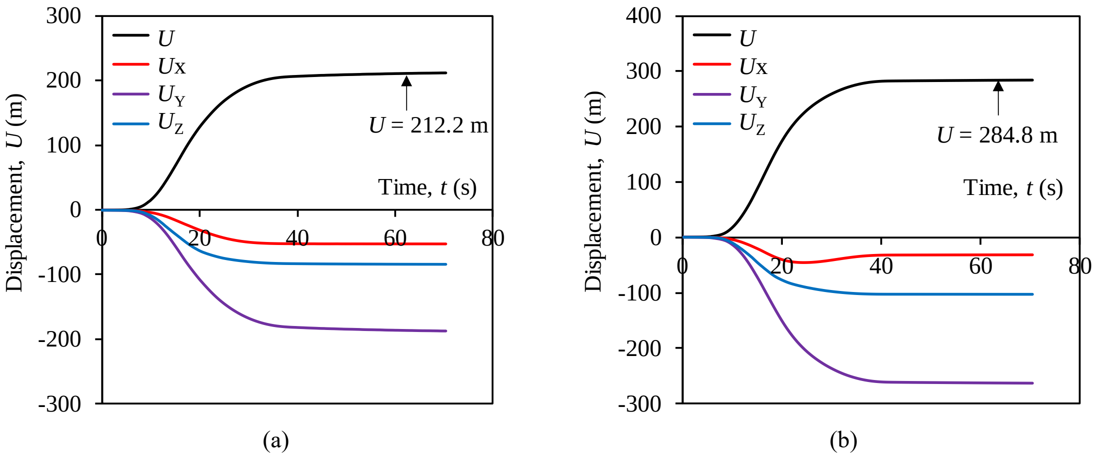

Fig. 17 Displacement evolution of the reference points (P_1 and P_2) within the failed mass: (a) reference point P_1; (b) reference point P_2.

Fig. 19(a) illustrates the landslide profiles at different moments, depicting the transition from the initial state to the final deposition. The runout path (red lines) can be determined based on these profiles, as shown in Fig. 19(b). Additionally, the affected area (black dotted curves) of the Lomba landslide can be accurately estimated by depicting the envelop of the profiles of the failed mass, as shown in Fig. 19(b). The results highlight the capability of the CEL method to accurately predict the landslide's runout path, affected areas, and deposition profile—critical elements for geotechnical engineering and disaster mitigation. Such predictive models enable engineers and decision-makers to optimize land-use planning, design effective protective structures, and implement early warning systems. By anticipating the extent of potential landslides, resources can be strategically allocated to high-risk areas, minimizing infrastructure damage and reducing the potential for loss of life and property.

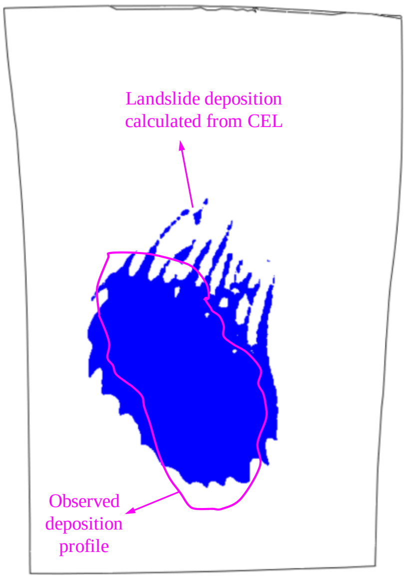

Fig. 18 Comparison of the deposition profile with the observed topography after the Lomba Grande landslide

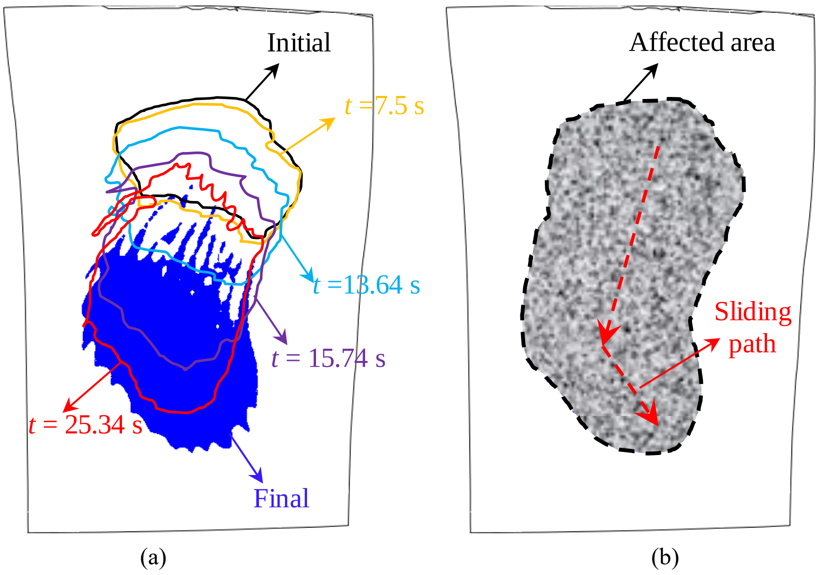

(a) (b)

Fig. 19 The evolution of the profiles of the failed mass and the affected area of the landslide: **(a)** profiles of the failed mass at different moments; **(b)** the affected area of the landslide.

5. Conclusions and implications

This study investigates the earthquake-triggered Lomba Grande landslide and its runout behavior by conducting CEL large-deformation modeling, incorporating the actual slope geometry and the earthquake loading. The characteristics of landslide runout behavior, such as runout distance, landslide velocity, the morphology of shear bands, affected area, and the final deposits, are explored in detail by the CEL. The comparison between the observed and calculated results provides some practical insights for rock slope engineering. Significant key findings and practical implications of this work are summarized below:

(1) **High kinetic-energy landslide with fast movement:** The numerical results indicate that the Lomba Grande landslide is a high-energy geo-disaster, characterized by extremely rapid movement of the failed mass, reaching a maximum sliding velocity of approximately 46.1 m/s. Such rapid mass movement can overwhelm traditional landslide barriers, requiring alternative mitigation strategies, such as energy dissipation structures, flexible barriers, or improved slope stabilization techniques. **Practical implication:** Furthermore, numerical models that fail to account for high-velocity landslides risk underestimating runout distances and impact forces, potentially leading to inadequate hazard zoning, insufficient evacuation planning, and miscalculated engineering safety margins. This underscores the importance of integrating dynamic landslide modeling techniques in disaster risk assessment to ensure more accurate forecasting and effective mitigation planning.

(2) **Significant plastic dissipation:** The plastic strain is initially developed in the area in contact with the base rock, then in the upper region of the failed mass. The highest plastic strain values develop along the interface between the failed mass and the base rock. As the failed mass moves, plastic strain within the rock accumulates, leading to the significant dissipation of the plastic strain energy along with the long-distance runout process. This gradually reduces energy and controlling runout distance. Numerical models that fail to account for both initial acceleration and plastic dissipation risk either underestimating the impact forces or overestimating the final travel distance. **Practical implication:** Accurate simulation of the interaction between the failed mass and the base rock is a bias towards to the effective estimation of the dissipation of the plastic strain energy and the long-distance runout process. To improve risk assessments and mitigation strategies, models must integrate both kinetic and plastic dissipation effects to predict runout behavior accurately.

(3) **Ability of CEL to capture the runout behavior and deposition topography:** The analysis shows that the numerical results are consistent with those observed characteristics in the 2D slope section and 3D deposition profile, indicating a coincidence in the initial failure surface, the runout distance and the final deposition topography. Particularly, the failed mass first shifts toward the left side and subsequently moves toward the right side of the base rock, primarily due to the effect of the local topography. **Practical implication:** This discovery first demonstrates that the CEL is a powerful tool capable of simulating the large-scare landslide and capturing the complex deposition topography. However, the real-world landslide is heavily dependent on the complex topography. The assumption of an ideal slope without considering the practical geometry may deviate from reality, which highlights the significance of including complex real-world slope topography. To enhance the reliability of landslide risk assessments, high-resolution topographic data (e.g., LiDAR, remote sensing, or photogrammetric surveys) should be integrated into numerical models. This is particularly critical for regions prone to large-scale seismic-induced landslides, where complex topography dominates runout direction, velocity distribution, and deposition patterns.

(4) **The superiority of 3D large-deformation modeling in estimating the affected area and runout path:** The 3D large-deformation analyses allow a more authentic estimation of the movement path of the failed mass and its evolution during the runout process. A general consistency between observed and calculated areas implies that the CEL-LDFE model adequately reproduces the affected area of the landslide. **Practical Implication:** This highlights the importance of adopting 3D modeling techniques in engineering and planning practices to enhance the prediction and management of landslide hazards. By incorporating the full complexity of landslide mechanics, 3D models enable more accurate risk assessments. Engineers and planners can predict with greater confidence where landslides are likely to occur, how far the landslide might travel, and what areas are at the highest risk of impact. This can lead to improved land use strategies, such as restricting certain types of development in high-risk areas or implementing specific zoning regulations to minimize potential damage. Authorities can use data from 3D models to develop more targeted evacuation plans and response strategies.

6. Limitations

CEL-LDFE analyses have been successfully conducted to predict the earthquake-triggered landslide runout process. To further enhance the model's applicability to actual scenarios, suggested future research should focus on the following two directions:

(1) **Incorporating inherent variability of volcanic rock mass:** Volcanic formations typically exhibit sizeable natural variability of lithological formations and heterogeneities, with cohesion and friction angle typically exhibiting significant spatial variability. Overlooking the non-uniformity of rock properties may overestimate the slope

stability and underestimate the landslide risk. Therefore, incorporating spatial variability of rock mass enables a more precise simulation of earthquake-induced instability and displacement of rock slopes in the future.

(2) **Unknown sliding surface:** The failure surface is determined by comparing the slope topography before and after the landslide and is explicitly defined in the current large-deformation models. Further work should be conducted to evaluate whether the CEL approach can automatically detect the sliding surface by comparing the numerical failure surface with the observed one. This improvement allows a general consideration in earthquake-triggered landslide modeling, as the failure surface is unknown before the landslide event.

Notation

Acceleration	a_i
Body force	b_i
Material waves in CEL	c_d
Young's modulus	E
Variables in CEL method	f
Element size	L_e
Penalty stiffness coefficient in CEL	k_i
Source term in CEL	S
Time	t
Displacement of reference point	U_RP
Friction angle	φ
Dilatancy angle	ψ
Material density	ρ
Unit weight	γ
Value of Poisson's ratio	v
Tangential contact force	τ_i
Normal contact force in CEL	σ_i
Flux function in CEL	Ψ
Penetration displacement of Lagrangian body into Euler body	Δx
Critical incremental step in CEL	Δt_crit
Two-dimensional	2D
Three-dimensional	3D
Arbitrary Lagrangian-Eulerian method	ALE
Coupled Eulerian-Lagrangian approach	CEL
Digital elevation method	DEM
Euler volume fraction	EVF
Large-deformation finite element	LDFE
Material point method	MPM
Peak ground acceleration	PGA
Peak ground velocity	PGV
Rock Mass Rating	RMR
Remeshing and interpolation technique with small strain	RITSS
Volcanic Rock System	VRS

Author contributions

Xuejian Chen: Investigation, Methodology, Software, Formal analysis, Visualization, Writing - original draft, Writing - review & editing. **Fabricio Fernández:** Investigation, Software, Visualization, Writing - review & editing. **Euripides Vargas:** Software, Visualization. **Carlos Sousa Oliveira:** Investigation, Writing - review & editing. **Miguel Inácio:** Writing - review & editing. **Luis Ribeiro e Sousa:** Conceptualization, Writing - review & editing. **Ana Malheiro:** Writing - review & editing**. Rita Leal Sousa:** Formal analysis, Validation, Supervision, Writing - review & editing.

Conflicts of interest

The authors declare that they have no known interests that could have appeared to influence the work reported in this paper.

Acknowledgements

This research is supported in part by the Sand Hazards and Opportunities for Resilience, Energy, and Sustainability (SHORES) Center, funded by Tamkeen under the NYUAD Research Institute Award CG013. Carlos Sousa Oliveira is grateful for the Portuguese Foundation for Science and Technology´s support through partial funding UIDB/04625/2020 from the research unit CERIS.

References

Bandara, S., Ferrari, A., & Laloui, L. (2016). Modelling landslides in unsaturated slopes subjected to rainfall infiltration using material point method. *International Journal for Numerical and Analytical Methods in Geomechanics*, 40(9), 1358-1380.

Benson, D.J. (1992). Computational methods in Lagrangian and Eulerian hydrocodes. *Computer Methods in Applied Mechanics and Engineering*, 99(2), 235-394.

Benson, D. J., & Okazawa, S. (2004). Contact in a multi-material Eulerian finite element formulation. *Computer methods in applied mechanics and engineering*, 193(39-41), 4277-4298.

Chen, X.J., Li, D.Q., Tang, X.S., & Liu, Y. (2021a). A three-dimensional large-deformation random finite-element study of landslide runout considering spatially varying soil. *Landslides*, 18, 3149-3162.

Chen, X.J., Han, C.C., Liu, J., & Hu, Y.X. (2021b). Interpreting strength parameters of strain-softening clay from shallow to deep embedment using ball and T-bar penetrometers. *Computers and Geotechnics*, 138, 104331.

Chen, X.J., Hu, Y., Zhang, L., & Liu, Y. (2023a). 3D large-deformation modelling on face instability and sinkhole formation during tunnelling through non-uniform soils. *Tunnelling and Underground Space Technology*, 134, 105011.

Chen, X., Cheng, P., & Liu, Y. (2023b). Large-deformation finite-element analysis of square foundations in spatially variable sediments. *International Journal of Geomechanics*, 23(8), 04023128.

Chen, X., Ren, S., Yao, K., & Sousa, R. L. (2025). Large-deformation finite-element modeling of seismic landslide runout: 3D probabilistic analysis with cross-correlated random field. *Journal of Rock Mechanics and Geotechnical Engineering*, 17(1), 385-398.

Cheng, P., Liu, Y., Hu, J., Fang, K., & Hu, Y. (2025). Experimental study on dynamic response and failure mode of bedding rock slope with cracks under earthquake. *Bulletin of Engineering Geology and the Environment*, 84(2), 81.

Dassault Systémes. (2018). Abaqus analysis users' manual, version 2018.

Fernández, F., Rojas, J. E., Vargas Jr, E. A., Velloso, R. Q., & Dias, D. (2021). Three-dimensional face stability analysis of shallow tunnels using numerical limit analysis and material point method. *Tunnelling and Underground Space Technology*, 112, 103904.

Fernández, F., Vargas Jr, E., Muller, A. L., Sousa, R. L., & e Sousa, L. R. (2024). Material point method modeling in 3D of the failure and run-out processes of the Daguangbao landslide. *Acta Geotechnica*, 4277-4296.

Fernandez, F., Oliveira, C. S., Vargas, E., Sousa, L. R., Malheiro, A., Chen, X., Amaral, P., Moniz, L., & Sousa, R. L. (2025). Seismic Stability Assessment of Volcanic Slopes: A Case Study from São Miguel Island, Azores. *Rock Mechanics and Rock Engineering*. doi.org/10.1007/s00603-025-04404-z.

Guo, X., Fan, N., Liu, Y., Liu, X., Wang, Z., Xie, X., & Jia, Y. (2023). Deep seabed mining: Frontiers in engineering geology and environment. *International Journal of Coal Science & Technology*, *10*(1), 23.

He, M., Sousa, L. R., Müller, A., Vargas Jr, E., Sousa, R. L., Oliveira, C. S., & Gong, W. (2019). Numerical and safety considerations about the Daguangbao landslide induced by the 2008 Wenchuan earthquake. *Journal of Rock Mechanics and Geotechnical Engineering*, *11*(5), 1019-1035.

Hu, Y., & Randolph, M. F. (1998). A practical numerical approach for large deformation problems in soil. *International Journal for Numerical and Analytical Methods in Geomechanics*, 22(5), 327-350.

Islam, N., Hawlader, B., Wang, C., & Soga, K. (2018). Large-deformation finite-element modelling of earthquake-induced landslides considering strain-softening behaviour of sensitive clay. *Canadian Geotechnical Journal*, 56(7), 1003-1018.

Li, X., Tang, X., Zhao, S., Yan, Q., & Wu, Y. (2021). MPM evaluation of the dynamic runout process of the giant Daguangbao landslide. *Landslides*, 18, 1509-1518.

Liu, J., Chen, X., Han, C., & Wang, X. (2019). Estimation of intact undrained shear strength of clay using full-flow penetrometers. *Computers and Geotechnics*, 115, 103161.

Liu, X., Wang, Y., & Li, D. Q. (2020). Numerical simulation of the 1995 rainfall-induced Fei Tsui Road landslide in Hong Kong: new insights from hydro-mechanically coupled material point method. *Landslides*, 17, 2755-2775.

Liu, Y., Chen, X., & Hu, M. (2023). Three-dimensional large deformation modelling of landslides in spatially variable and strain-softening soils subjected to seismic loads. *Canadian Geotechnical Journal*, 60, 426-437.

Liu, Y., Cheng, P., Liu, E., Hu, J., Cheng, Y., & Su, L. (2024). Seismic response and dynamic failure mode of a class of bedding rock slope subjected to freeze–thaw cycles. *Rock Mechanics and Rock Engineering*, 1-19.

Miranda, T., Sousa, L. R., Gomes, A. T., Tinoco, J., & Ferreira, C. (2018). Geomechanical characterization of volcanic rocks using empiric systems and data mining techniques. *Journal of Rock Mechanics and Geotechnical Engineering*, 10, 138-150.

Nazem, M., Sheng, D., & Carter, J. P. (2006). Stress integration and mesh refinement for large deformation in geomechanics. *International Journal for Numerical Methods in Engineering*, 65(7), 1002-1027.

Nazem, M., Sheng, D., Carter, J. P., & Sloan, S. W. (2008). Arbitrary Lagrangian–Eulerian method for large-strain consolidation problems. *International Journal for Numerical and Analytical Methods in Geomechanics*, 32(9), 1023-1050.

Noh, W.F. (1964). A time dependent, two space dimensional, coupled Eulerian-Lagrange code. *Methods in Computer Physics*, 12-23.

Oliveira, C.S. (1992). Quantification of the seismic movement during the earthquake of January 1st, 1980. In Monograph 10 Years after the Azores earthquake of January 1st, 1980. Technical-Scientific Aspects, 1, 83-126, SRHOP/LNEC. (In Portuguese)

Oliveira, C.S., Nunes, J.C., Ferreira, M.A. (2008). Notes on the assessment of geological hazards in the islands of Faial and Pico following the earthquake of July 9, 1998. In Earthquake 1998. Azores, A decade later. 379-384. (In Portuguese).

Qiu, G., Henke, S., & Grabe, J. (2011). Application of a Coupled Eulerian–Lagrangian approach on geomechanical problems involving large deformations. *Computers and Geotechnics*, 38(1), 30-39.

Ren, S.P., Chen, X.J., Ren, Z.L., Cheng, P., & Liu, Y. (2023). Large-deformation modelling of earthquake-triggered landslides considering non-uniform soils with a stratigraphic dip. *Computers and Geotechnics*, 159, 105492.

Ren, S.P., Li, Y., Chen, X.J., Cheng, P., Liu, F., & Yao, K. (2025). Large-deformation insights into seismic landslide runout considering uncertainties in soils and ground motions. *Bulletin of Engineering Geology and the Environment*, 84, 1-18.

Sousa, R. L., Tinoco, J., Sousa, L. R., Karam, K., & Gomes, A. T. (2021). Volcanic rocks characterization based on soft computing algorithms by using VRS empirical system. In *ISRM International Workshop on Rock Mechanics and Geoengineering in Volcanic Environments*.

Sousa, R. L., Karam, K., & Einstein, H. H. (2014). Exploration analysis for landslide risk management. *Georisk: Assessment and Management of Risk for Engineered Systems and Geohazards*, 8(3), 155–170.

Sousa, R., Karam, K. S., Costa, A. L., & Einstein, H. H. (2016). Exploration and decision-making in geotechnical engineering – a case study. Georisk: *Assessment and Management of Risk for Engineered Systems and Geohazards,* 11(1), 129–145.

Valadao, P., Gaspar, J. L., Queiroz, G., & Ferreira, T. (2002). Landslides density map of S. Miguel Island, Azores archipelago. *Natural Hazards and Earth System Sciences*, 2(1/2), 51-56.

Wang, D., Bienen, B., Nazem, M., Tian, Y., Zheng, J., Pucker, T., & Randolph, M. F. (2015). Large deformation finite element analyses in geotechnical engineering. *Computers and geotechnics*, 65, 104-114.

Zang, M.D., Yang, G.X., Dong, J.Y., Qi, S.W., He, J.X., & Liang, N. (2022). Experimental study on seismic response and progressive failure characteristics of bedding rock slopes. *Journal of Rock Mechanics and Geotechnical Engineering*, 14, 1394-1405.

Zhao, B., Su, L.J., Wang, Y.S., Li, W.L., & Wang, L.J. (2023). Insights into some large-scale landslides in southeastern margin of Qinghai-Tibet Plateau. *Journal of Rock Mechanics and Geotechnical Engineering*, 15, 1960-1985.